Deformable Haptic Model Generation Through Manual Exploration

Orcun Goksel* Seokhee Jeon*+ Matthias Harders* Gábor Székely*

*Computer Vision Laboratory, ETH Zürich, Switzerland
+Department of Computer Engineering, Kyung Hee University, South Korea

ABSTRACT

Interaction with virtual deformable models is common in several haptic contexts, such as in medical training simulators. This paper presents a methodological procedure for the creation of such virtual models from their real-life counterparts. Both the surface geometry and the elastic parametrization of an object are reconstructed from position/force readings during an operator-assisted exploration of the object. A 3D mesh model is then generated from the surface contact points. The internal elastic modulus is found using the 3D finite element method. This modeling method is compared with two common 1D elastic models, namely Kelvin-Voigt and Hunt-Crossley. Results using three deformable homogeneous silicone samples show successful geometry reconstruction. 1D model parameterizations exhibit high variation dependent on geometry and contact location. In contrast, elastic modulus reconstruction yields a global model parameterization independent of geometry. Elastic moduli estimated in experiments correlated with their known values, and were shown to be reproducible among samples with different geometries.

1 INTRODUCTION

For the haptic rendering of real-life objects in virtual environments, haptic modeling has always been an active interest of research. Virtual deformable models are an essential part of many haptic applications, consequently they have been widely studied for model generation. Because the extent of an object is crucial to identify contacts in virtual rendering, geometric modeling does often go hand in hand with haptic modeling in this context. Therefore, the term *modeling* is commonly used in relation to either the geometry/shape or (visco)elastic parameterization of an object, both of which are indeed required for a realistic haptic simulation. In this work, we address both aspects of modeling in an integrated framework.

There are commonly two modeling approaches: manual and automatic reconstruction of objects. Here, *manual* refers to defining the object geometry implicitly as a combination of geometric primitives, such as planes, cubes, and spheres. Also, prior knowledge on the haptic characteristics of the object is required for haptic rendering. Then, one can describe the virtual object and its contact behaviour; e.g., for a virtual half-sphere, applying an outward force as a known (assumed) function of penetration depth can simulate one common type of penetration-dependent elastic interaction with this particular geometry. Programming such models manually for real-life complex objects can be a time-consuming task and often is not straight-forward. Moreover, interaction response from a real object is in general not merely a function of penetration depth as in the simple example above, but is often a complex outcome of its entire shape, material properties, and *boundary constraints* (how it is fixated in space, such as standing on a tabletop). Consequently, except in simple interaction scenarios, virtual model generation relies on automatic data-driven methods. 3D scanning, such as using laser or visible light, is the most popular data acquisition method. However, this method requires additional equipment. Also, when haptic modeling is performed in a different coordinate frame than shape modeling (for instance, laser surface scanning followed by haptic/indentation data collection), this approach involves the post-registration of scanned geometric models to the haptic coordinate frame for correctly projecting the haptic model data onto the geometric model. If haptic rendering is to be performed on a different device/location, such model needs to be eventually brought into the rendering coordinate frame. These all hinder the modeling-to-rendering pipeline greatly in practical scenarios. Any registration errors in this pipeline, despite common approaches such as tracking with markers, will generate inconsistent haptic rendering. There is an evident benefit from simpler, robust techniques for model acquisition. To avoid additional equipment and complexity, we exploit the haptic device itself in entire model generation. This eliminates the need for registration, integrating both geometric and elastic modeling aspects into a single procedure.

Several touch-based solutions for collecting spatial points for geometry reconstruction were proposed in the literature, e.g. [23] and the commercial products MicroScribe[1], Romer[2], Nikon[3], etc. There have also been studies combining visual scanning for geometry modeling and haptic probing for viscoelastic modeling [16]. In this paper, we present the concurrent generation of both models for deformable media from haptic interaction data during manual exploration of the object to be modeled. For shape generation, we first identify the contact points and then employ a sparse point surface reconstruction method. The convex hull of Delaunay triangulation provides a robust and computationally-efficient technique for surface extraction from our convex synthetic models [1].

Due to the deformable characteristic of soft tissue, deformable modeling has been a major focus for medical simulations [2, 21]. To compute indentation forces in haptics, due to real-time rendering constraints, it has been proposed to use 1D viscoelastic approximations, variations of spring-damper models such as Kelvin-Voigt, Maxwell, and Hunt-Crossley models [9]. There have also been studies on experimental validation of such different parameterizations [22]. These models are effective for accurately describing the contact response at a particular location. Nevertheless, they are not suitable for simulating complex object behaviour in virtual environments; because such 1D model parameters do not indicate any physical material property, but they are instead an aggregate outcome of the shape, size, and placement of the object, together with its physical properties. Then, the modeled parameter is also a function of spatial contact location, and not only an internal change of underlying material physics. For instance, if a standing deformable object is probed laterally near its base and further above at the top, different force-displacement profiles will be observed, even when the material is homogeneous, due to the former interaction being

ogoksel@vision.ee.ethz.ch
jeon@khu.ac.kr
mharders@vision.ee.ethz.ch
szekely@vision.ee.ethz.ch

[1] http://www.emicroscribe.com/
[2] http://us.romer.com/
[3] http://www.nikonmetrology.com/

closer to its fixed (zero-displacement) base. To cope with this, sophisticated data-driven spatial model parameterizations have been proposed [10], however those rely on a large number of collected samples and a proper interpolation scheme for rendering.

An alternative approach is to use continuum mechanics with an inherent geometric representation, which is often in the form of a *mesh* – a spatial discretization of the continuum. Several continuum mechanics representations for tissue have been proposed and studied in the literature [7]. The Finite Element Method (FEM) is a popular technique particularly in medical applications, due to its ability to model complex shapes and interactions. FEM can inherently accommodate for geometry and boundary conditions, the relative locations of which with respect to an interaction point are known to significantly affect the nature of deformation [14]. Considering soft tissue deformation in medical simulations, such boundary constraints are often the bones, as they are relatively rigid and are *grounded* through the skeletal system, e.g., to the patient's bed. Accordingly, reconstructing the location of such fixed constraints is an essential aspect of geometric model generation. These constraints together with the elastic properties of the object and its overall geometry gives rise to the observed kinesthetic forces when the object is probed. Such probing is indeed commonly utilized by medical practitioners to resolve for the underlying elasticity, as in palpation examinations of breast tumors, prostate cancer, and liver cirrhosis.

Elastography, which is the viscoelastic parameter identification of soft tissues, is an active area of research [5, 6, 11, 24]. Common techniques rely on imaging dense internal tissue motion using MR or ultrasound. Indeed, elastic parameter estimation from force/displacement readings with single-point interaction is not straightforward [15]. We demonstrate this for homogeneous objects when the entire object geometry can also be estimated concurrently.

Several sophisticated nonlinear and dynamic FEM methods have been investigated in the literature [5, 6, 12, 18, 20]. A novel FEM reconstruction method is not the focus of this paper. We accordingly use a linear isotropic model that is fast both for parameter reconstructions and also for potential subsequent haptic rendering using the same model with estimated parameters. Viscoelastic tissue characterization was proposed in [20] using resonant amplitude/frequency shift of a torsional oscillator coupled to skin. However, this requires specialized hardware and only the superficial tissue layer can be measured. In [3], surface points tracked by cameras were used for modeling deformable objects through interpolations in the strain-space of an underlying assumed FEM model. Time-varying surface profiles during aspiration of tissue were utilized in [12] for viscoelastic characterization. In contrast to such camera-based surface tracking approaches, we herein estimate parameters merely from the displacement and force at a single contact. Similarly, a robotic indenter was used in [18] for viscoelastic tissue characterization from time-series force readings; nevertheless, this method considers only local deformations and it does not address geometric model generation.

In this work, we present the construction of geometric and haptic models from several single-contact interactions. We demonstrate the use of FEM for elastic modulus estimation with homogeneous objects. We also identify interaction parameters from 1D viscoelastic contact models, and compare those with elastic moduli while indicating the separate natures of these two modeling approaches. A discussion is provided at the end.

2 METHODS

We first introduce our naming convention for the object geometry, which can be followed in the cross-sectional view of a synthetic model in Fig. 1(a). The surface S defines the interface where one can interact with the object. The boundary B is the side of the object that is not directly visible and/or be interacted with. The boundary also fixates the deformable object in space. The mesh M

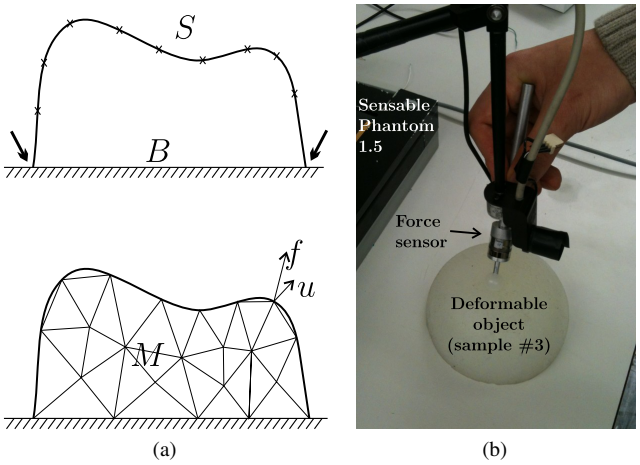

Figure 1: (a) A 2D sketch illustrating the contact points on a surface and an FEM mesh model of the object. (b) Our experimental setup.

is an internal spatial discretization of the object into geometrical primitives such as tetrahedra and hexahedra.

For visual rendering, contact handling and 1D viscoelastic models, the outer surface S is the only relevant geometry component and hence shape modeling in those contexts refers to the recovery of that surface alone. Nevertheless, with continuum mechanics a boundary definition is required to determine contact behaviour. FEM also requires a mesh discretization of the object volume to integrate such continuum effects over simplex geometric primitives. We construct the geometric and the elastic models through manual haptic exploration of the object. We use a haptic device for this purpose while recording positions and forces at the device tip. We later process this data offline for both geometric and haptic model generation. In this paper, we use a Sensable Phantom 1.5 device instrumented with an ATI Nano17 force sensor. Our data acquisition setup during one sample palpation is seen in Fig. 1(b).

Our haptic exploration involves two phases: (I) is to identify the object extent and the boundary B, and (II) is to identify the surface S and the elastic parameterization. Since B is not visible or accessible, we infer it from its perimeter around the object shown with the arrows in the 2D model in Fig. 1(a). In 3D, this is the circumference around the object at its fixed plane/surface. We thus first simply delineate the object around its base with the haptic tool. An analogy for a breast palpation examination, in which the ribs are the nearest bones enforcing boundary constraints, would be the tracking of the ribs around the breast with the tool. Subsequently, the object surface is probed (palpated) at multiple locations with the haptic device. From palpations, first individual contacts are isolated using a finite-state machine contact model. From initial contact points, the surface S is approximated. From B and S, which together indicate the object outline, a mesh M is then generated for the object.

2.1 Boundary Approximation and Contact Detection

The acquired forces and displacements are first zero-phase low-pass filtered to remove high-frequency noise in the data. Fig. 2 shows the force magnitude profile from a sample experiment. The first part of the interaction, phase I, is the fixed boundary exploration (in our case the rigid table surface) and the latter peaks are the palpations in phase II. Once the contact in phase I is easily extracted automatically, the circumference of the object is identified from the path of the 3D tool position in this phase. This is shown with the circular curve for the half-sphere model in Fig. 3(a). The curve is then down-sampled using *farthest-point sampling*, which starts by

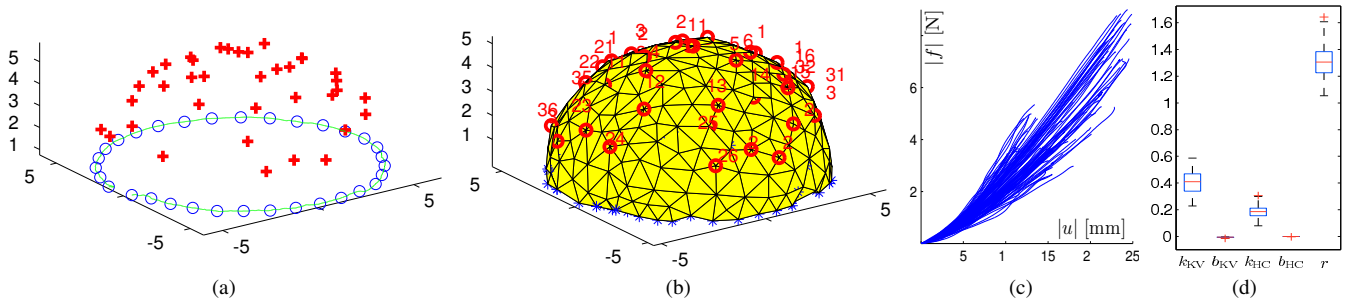

(a) (b) (c) (d)

Figure 3: Geometric model generation. (a) Detected contact points (+) and the object base circumference, marked with circles after down-sampling. (b) Surface of the resulting mesh, also showing the zero-displacement FEM nodes (∗). The FEM nodes (○) closest to each contact are used for deformation simulation of that particular contact. (c) Displacement-force profiles of palpations on a *homogeneous* block-shaped sample. (d) Distribution of identified parameters for the Kelvin-Voigt and Hunt-Crossley models for a cylindrical elastic sample.

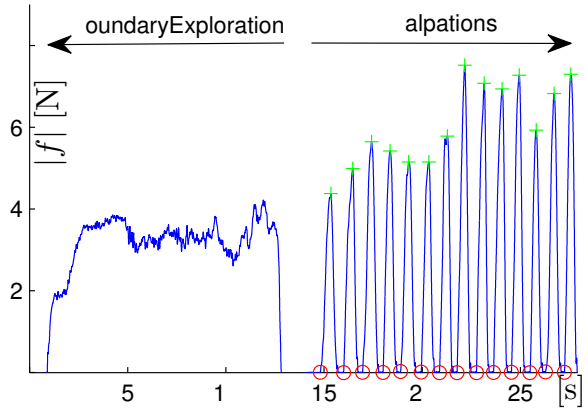

Figure 2: Sample force magnitude profile with detected contacts (○) and peak interaction forces (+).

picking a random location on the tool path and adding it to a set of sampled-points set. Then, at every iteration, the distances from all points to this sampled set are computed and the furthest path point is chosen to be added to the set of sampled points. This is repeated until no part of the path is further to the sampled points than a predefined threshold d. Let P_B be the 3D locations of the resulting sampled points as shown with the circles on the curve in Fig. 3(a).

The instants of palpations in phase II of an interaction are detected automatically from the force magnitude profile using a finite state machine. The *contact* state is activated at a force threshold of τ. In order to detect the initial contact, the first time instant that the force started increasing is then backtracked. Sample detected instants are shown in Fig. 2. The contact state is deactivated when the force magnitude is negligible. Let P_S be the 3D locations of initial contacts shown with plus signs (+) in Fig. 3(a).

2.2 Surface Reconstruction and Volumetric Meshing

The set of points $P_B \cup P_S = P$ form a 3D sparse sampling of the object outline, and is used used for surface reconstruction to determine an approximate object shape. For a convex object, the *convex hull* of P gives the surface of such object. This can be computed as a byproduct of the Delaunay triangulation of a 3D point cloud [1]. Then, the surface S is extracted in the form of triangular facets. These convex-hull extracted surface triangles are often of *poor quality* to be used in an FEM mesh. The quality of an element (triangle/tetrahedron) is measured by certain aspect ratio criteria [19]. Common meshing algorithms do not change explicit surfaces that are given as inputs [8]. Thus, to avoid such degenerate faces in the mesh, we go through a volumetric (voxel) representation of the object. To mesh the volume, we use the technique of Boissonnat and Oudot [4] implemented in the Computational Geometry Algorithms Library (CGAL)[4]. To that end, we first discretize the bounding box of S on a 3D Cartesian grid, each voxel of which is labeled as being inside/outside of this surface. Subsequently, CGAL meshes this label grid into a tetrahedral discretization. It generates uniform tetrahedra that are of given size ℓ and that are bounded by a given radius-edge ratio ρ while approximating a given surface with a distance error σ. The surface of a sample mesh is seen in Fig. 3(b). Finally, the contact locations P_S are cast onto the nearest mesh nodes for performing the FEM analysis. These are circled in Fig. 3(b) with numbers indicating their palpation order.

2.3 Uniaxial Elastic Modeling

For viscoelastic modeling, we compare two popular 1D models, namely Kelvin-Voigt and Hunt-Crossley, with the 3D FEM model. For the 1D models, first the displacement-force profile of each palpation is extracted; see Fig. 3(c) for an example. The Kelvin-Voigt model explains the relationship between displacement u and force f with two parameters as follows:

$$f = k_{KV}\, u + b_{KV}\, \dot{u} \tag{1}$$

whereas the Hunt-Crossley model uses three parameters:

$$f = k_{HC}\, u^r + b_{HC}\, u^r\, \dot{u} \tag{2}$$

where k and b are, respectively, the stiffness and the damping terms. Then, for a given palpation (given set of multiple u and f pairs, denoted by the vectors $\mathbf{u}$ and $\mathbf{f}$), Kelvin-Voigt parameters are given by the solution of the following least-squares problem:

$$\underset{k_{KV},\, b_{KV}}{\arg\min} \left| [k_{KV}\ b_{KV}][\mathbf{u}\ \dot{\mathbf{u}}]^T - \mathbf{f} \right|^2 . \tag{3}$$

It was shown recently in [9] that the Hunt-Crossley parameters can also be identified similarly. To that end, an assumption is made that the interaction speed is small relative to the stiffness-to-damping ratio, i.e. $|\dot{\mathbf{u}}| < \frac{0.1 k_{HC}}{b_{HC}}$. This is reasonable for manual interaction velocities, and also because the damping in our models are minuscule as shown later. The logarithm of (2) aggregated for the full palpation extent yields the following least-squares problem [9]:

$$\underset{c_1, c_2, c_3}{\arg\min} \left| [c_1\ c_2\ c_3][1\ \dot{\mathbf{u}}\ \ln(\mathbf{u})]^T - \ln(\mathbf{f}) \right|^2 \tag{4}$$

[4] http://www.cgal.org/

from which the parameters can be extracted subsequently such that $k_{\mathrm{HC}} = \mathrm{e}^{c_1}$, $b_{\mathrm{HC}} = \mathrm{e}^{c_1} c_2$, and $r = c_3$.

Distribution of parameters identified as above is given in Fig. 3(d) for a cylindrical phantom. Damping effect is seen to be negligible for the materials we use. We thus also use the two following modified models without damping:

$$f = k_{\mathrm{V}}\, u\,, \tag{5}$$

$$f = k_{\mathrm{C}}\, u^{r}\,. \tag{6}$$

We identify these new parameters similarly from experimental data.

2.4 3D FEM Modeling

To accommodate for complex 3D geometries, we also use the FEM with a linear stress-strain Hookean model. For a mesh with n nodes, FEM relates the nodal displacements $\mathbf{u} = [u_1^{\mathrm{x}}\, u_1^{\mathrm{y}}\, u_1^{z}\, u_2^{\mathrm{x}} \ldots u_n^{z}]^{\mathrm{T}}$ to corresponding internal nodal forces $\mathbf{f}$ through a $3n \times 3n$ sparse stiffness matrix as $K\,\mathbf{u} = \mathbf{f}$. Considering the negligible viscous effects observed for our model above in Fig. 3(d), we omit damping here. Without loss of generality, we assume a node numbering (permutation) with the nodes on boundary B listed at the end. Since the displacement on B is always zero, then K can be decomposed as:

$$\begin{bmatrix} K^{11} & K^{12} \\ K^{21} & K^{22} \end{bmatrix} \begin{bmatrix} \mathbf{u}^{1} \\ \mathbf{0} \end{bmatrix} = \begin{bmatrix} \mathbf{f}^{1} \\ \mathbf{f}^{2} \end{bmatrix} \tag{7}$$

$$K^{11}\,\mathbf{u}^{1} = \mathbf{f}^{1} \tag{8}$$

$$K^{21}\,\mathbf{u}^{1} = \mathbf{f}^{2}\,. \tag{9}$$

The forces on the right-hand-side describe the external forces on the model, whereas the left-hand-side represent the internal body forces. While the boundary forces $\mathbf{f}^2$ are not known, $\mathbf{f}^1$ is known at all times during a palpation. The three rows of $\mathbf{f}^1$ corresponding to the force on the palpated node are read from the force sensor. All other $\mathbf{f}^1$ components are zero as all other model nodes are free in space, i.e. f^1=$[0\,0 \cdots 0\, f^x\, f^y\, f^z\, 0 \cdots 0]^{\mathrm{T}}$. Accordingly, (8) is used to reconstruct elasticity [6]. For clarity, the superscripts ^{11} and ^{1} are dropped throughout the rest of this section.

K is built by the superposition of individual element stiffness matrices, which are for instance 12×12 for the four-node tetrahedral elements. Each element stiffness matrix K_e is an integration of the continuum Hookean model inside that element. Consequently, K_e is a function of that element geometry, spatial interpolation used, and the element elasticity. The elasticity is described by the Young's modulus (e) and the Poisson's ratio (η), which explain the elastic and the incompressibility components, respectively.

Human soft tissue is known to be nearly incompressible, due to its high water content. Then, for FEM parameter identification, typically a constant high η is assumed and only the elastic modulus e is sought. Fortunately, e appears linearly in element stiffness matrices K_e [25]. Then, the vector of all moduli $\mathbf{e}$ can be separated as a linear multiplier in (8) as follows:

$$\mathbf{K}_{\mathrm{G}}\,\mathbf{e}\,\mathbf{u} = \mathbf{f} \tag{10}$$

where $\mathbf{K}_{\mathrm{G}}$ is a tensor for stiffness that depends solely on the geometry, interpolation, and η, where the elastic moduli $\mathbf{e}$ are decoupled. It is basically composed of the matrices K_e before having multiplied with the Young's modulus.

Given dense displacement data $\mathbf{u}$ such as from medical imaging modalities as ultrasound or MR, it is possible to identify individual element parameters from (10) using static [11] or dynamic excitations [6]. However, since we only observe the displacement at the contact point itself, there is no straight-forward solution of reconstructing arbitrary elasticity distributions. Nevertheless, (10) can be solved for homogeneous models, for which there is a single modulus e to identify [17]. This then yields to:

$$K_{\mathrm{G}}\,(e\,\mathbf{u}) = \mathbf{f} \tag{11}$$

Table 1: Silicone samples used in the experiments.

Sample	Geometry	Known e [kPa]	Estimated e [kPa]
#1	cylinder of 40 mm radius and 80 mm height	29	28.73
#2	square block of $105\times105\times47$ mm^3	16	10.73
#3	(near) half-sphere of 60 mm radius and 55 mm height	16	11.31

with K_{G} is a *matrix* and e is a single value. Then, for a single palpation instance i using the FEM, the following least-squares problem gives a displacement prediction $\mathbf{u}_i^{\mathrm{pred}}$ at all nodes from the 3×1 force vector f_i^{meas} measured at the tooltip for that palpation:

$$\mathbf{u}_i^{\mathrm{pred}} = \arg\min_{u} |K_{\mathrm{G}}\,\mathbf{u} - \mathbf{f}_i^{\mathrm{meas}}|^2\,. \tag{12}$$

The three axial components of $\mathbf{u}_i^{\mathrm{pred}}$ that correspond to the palpated node i is the FEM predicted nodal displacement u_i^{pred} for that palpation. Let $3\times p$ matrix U_{pred} be the collocation of such displacement predictions from all palpations p of a sample, and U_{meas} be the corresponding measured displacements at those palpation instances. Then, from (11), $e\,U^{\mathrm{meas}} = U^{\mathrm{pred}}$ should hold. Thus, an e that fits all measurements in a least-square sense is found as follows:

$$e = U^{\mathrm{pred}}\,U^{\mathrm{meas}\mathrm{T}}\left(U^{\mathrm{meas}}\,U^{\mathrm{meas}\mathrm{T}}\right)^{-1}\,. \tag{13}$$

In order to assess the sensitivity of such modulus estimation to the number of observed palpations in our results, we also estimated a separate modulus e_i for each individual palpation i using solely the measured and predicted displacements from that particular palpation, $e_i = \mathbf{u}_i^{\mathrm{pred}}\,\mathbf{u}_i^{\mathrm{meas}\mathrm{T}}\left(\mathbf{u}_i^{\mathrm{meas}}\mathbf{u}_i^{\mathrm{meas}\mathrm{T}}\right)^{-1}$.

3 Results

We experimented with three different homogeneous silicone samples listed in Table 1. Haptic exploration of each sample took 1 to 2 minutes, generating 35 to 100 distinct contacts. The shapes were generated as described in Section 2.2. For contact detection and mesh generation, the parameters were set empirically such that the contact force threshold τ=1 N, the mesh size ℓ=10 mm, tetrahedra radius-edge ratio ρ=2, and the surface approximation threshold σ=2 mm. In FEM reconstruction, a Poisson's ratio η of 0.49 was used to achieve near-incompressibility. For each palpation, the data at 10 mm indentation was used for reconstruction by FEM in order to minimize noise in readings. The FEM solver was written in Matlab and was validated against Ansys results.

Damping was negligible for all samples, similarly to the cylinder sample shown in Fig. 3(d). Accordingly, parameters identified with no damping assumption are reported here. These include k_V of the modified Kelvin-Voigt model in (5) and k_C and r of the modified Hunt-Crossley model in (6); the distributions of which are shown for each palpation, respectively in Figs. 4(a) and 4(b). The spatial distribution of k_V is shown for sample #1 in Fig. 5(top) and for sample #2 in Fig. 5(middle). Note that the identified parameter is strongly dependent on the location of interaction. For instance, on the side of the cylindrical sample #1, the model indicates the "stiffness" getting lower as palpation point is further from the ground. This is obviously merely a side-effect of the geometry, and the fact that the cylinder is grounded (fixed in space) at its base. This geometry dependence of k_V is shown in Fig. 5(bottom-left).

The same geometry-dependent effect is also observed with the Hunt-Crossley model. Since it has two parameters k_C and r that both contribute to resultant force, this effect is difficult to demonstrate in the combined space of the two (especially, since r has a nonlinear effect). We thus used the average r for each sample shown

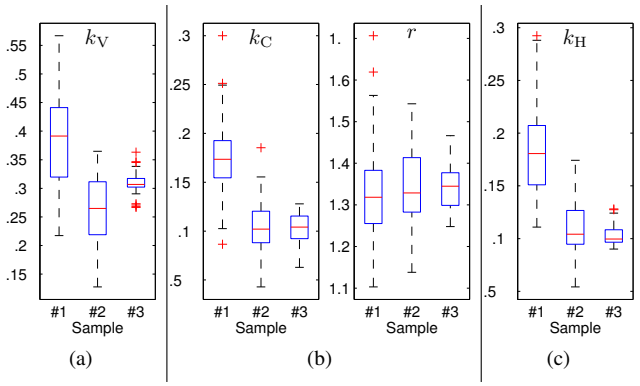

Figure 4: Distributions of estimated 1D model parameters using negligible damping assumption with the following models (a) Kelvin-Voigt, (b) Hunt-Crossley, and (c) Hunt-Crossley parameter re-identified at a fixed r per model (average from (b) was used).

in Fig. 4(b) as a constant parameter, to re-identify the elastic Hunt-Crossley component in (6), which we now call k_H to distinguish. It is plotted similarly in Fig. 5(bottom-center), exhibiting strong correlation with the palpated height.

The moduli identified for each homogeneous sample from (13) are given in Table 1. As seen, these are relatively close to the known sample construction values as the ground-truth. It is important to note that none of the 1D models above can produce such a physically-meaningful global model parameter that can be compared to a ground-truth fundamental material property. To show the sensitivity of moduli estimation to palpations performed per point, we also report the distribution of moduli in Fig. 6(a), if they were to be estimated separately for each palpation. In this plot, the globally-identified sample modulus is marked with $*$.

In Fig. 6(b), spatial distributions of individual modulus estimations are shown for two samples on their reconstructed surfaces. As seen in these figures, in contrast to 1D model parameters, the elastic moduli estimated by the FEM do not have a systematic dependence on palpation location. This is also observed in Fig. 5(bottom-right), where modulus-per-palpation is plotted against the contact point distance from the ground for the cylindrical sample #1.

Our implementation in Matlab, with the meshing performed by a compiled executable, runs offline in an automatic pipelined framework and can generate the entire model under 45 s on an Intel Core i7 2.66 GHz processor. For all models, extraction contacts from measurements took less than 10 s, identifying all 1D model parameters took less than 0.5 s, whereas the FEM modulus estimation took under 3 s including stiffness matrix K_G formation. The remaining time was spent on mesh generation, in particular labeling the discretized Cartesian grid inside the surface S.

4 Discussion

Our most notable result is the consistency and repeatability of the FEM estimated moduli. In particular, it is seen in Fig. 6(a) that the moduli of samples #2 and #3 were estimated very closely, even though those samples have significantly different geometry. Sample #1 modulus was identified correctly as being substantially higher than the other two. It is also worthwhile to note that none of the individual modulus estimations of the stiffer sample #1 was lower than any of the individual estimations of samples #2 and #3, which shows the robustness of the estimations. This clear separation between the first and the other two models is not observed with any of the other 1D model parameterizations.

Individual per-palpation modulus estimations have been presented in this paper merely to demonstrate any variability they

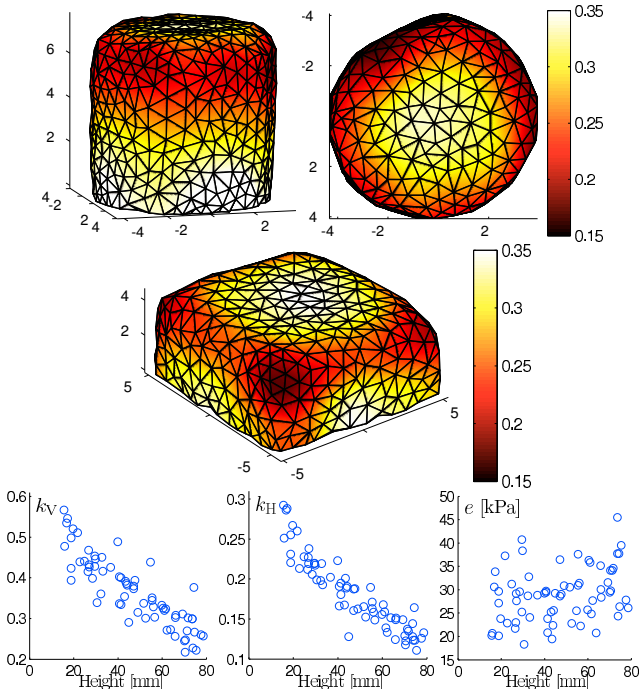

Figure 5: Spatial distribution of the identified k_V indicating its geometry dependence: (top) Sample #1 side and top view; (middle) sample #2 isometric view; and (bottom) parameters k_V, k_H, and per-palpation modulus e identified on the side of sample #1 as a function of height. Each surface was rendered using a radial-basis function interpolation of the estimated parameter values given at known palpation points.

may contain, which may occur due to noise in data collection and geometric model generation. Our proposed method indeed is to identify a common global modulus from all palpations together as presented in the methodology section. This enjoys the benefit of FEM reconstruction being a *model-based* approach by fitting several (geometry-compensated) data to a single model space. In contrast, no global model can be assumed with 1D techniques.

For surface extraction, we used convex hull since our synthetic models were convex in shape. Without any prior on convexity, one can resort to the more sophisticated *Poisson surface reconstruction*. From the point cloud P and the surface normals at each point, this method extracts the surface from an implicit surface representation generated by solving Poisson's equation [13]. Our preliminary results show that the contact normals can be approximated from palpations, such as the force direction at initial contact or the displacement at maximum indentation. Poisson reconstruction is also observed to be robust to noise in such normal estimation.

In order to demonstrate our modeling technique, we have used a haptic device for data collection since we readily had access to one in our group. Nevertheless, in principle any tool with integrated force and position sensing capabilities could be used.

The geometry reconstruction presented in this paper is not only required for virtual modeling, such as contact detection and graphical representation during rendering, but it is also an essential component for FEM modeling. Without knowing the extent of the object and its boundary constraints with reasonable certainty, FEM parameters could not be estimated reliably. Uniaxial approaches, however, do not require the geometry for force modeling. This has impacts on possible strategies for haptic rendering. Using 1D models, the interaction response in-between acquired contact points are typically interpolated. Although sophisticated interpolation methods exist, this still requires a relatively dense data collection as

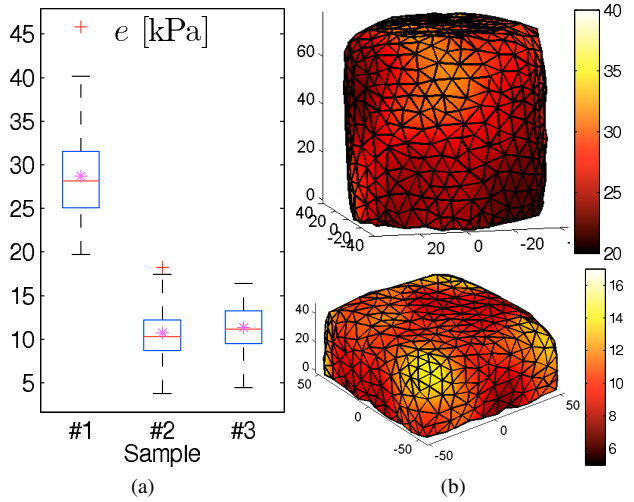

Figure 6: (a) Distributions of individual moduli estimations for each palpation, with $*$ marking the global parameter estimation. (b) Geometry reconstructions from samples #1 [top] and #2 [bottom] also showing spatial modulus distribution when e is identified separately for each palpation.

such models lose their predictive power away from the collected data points. For instance, when rendering force feedback from the cylinder sample #1 shown in Fig. 5(top-right), if no data had been collected near the center of its top surface, any interpolation using the data near the circumference would yield a twice softer than expected interaction. In contrast, haptic rendering using the FEM is inherently defined by (11). Once modulus is estimated, (11) can be solved at the time of rendering using the estimated modulus e and the palpation u to find the force feedback f. Although this can be an involved task to achieve in real-time, as long as the geometry is well-defined, interactions for a wide range of contact natures can be simulated. For instance, simulating multi-contact with FEM is then no different than single-contact, although this is not straightforward using 1D contact models. Haptic augmentation can also be handled implicitly by modifying the spatial FEM discretization. For instance, a stiffer inclusion can be simulated simply by changing the internal mesh and increasing the modulus of that location to desired value. In contrast, augmenting 1D models or their interpolations requires heuristic treatments. Concurrent generation of geometric and haptic models is not only relevant for virtual environments, but it is also essential in robotics, where both the geometry and the contact properties of an object need to be identified on-the-fly before a full-interaction such as grabbing. It can furthermore be beneficial as a quantitative diagnosis tool, e.g. for medical palpation examinations.

5 Conclusions

In this paper, we have presented a haptic modeling technique to reconstruct both the geometry and the deformable parameterizations of objects. We have compared 1D models and the 3D FEM for elastic modeling. The former are fast and simple, however, yield geometry-dependent results. The latter takes the geometry and the constraints into account, and solves for the elastic modulus, which is an absolute global elasticity measure that can be validated with object construction parameters and by independent indentation experiments. FEM modulus estimation has been shown to be repeatable within the same sample and among differently-shaped samples of the same material. Moduli were also significantly distinctive between samples made of different material. In the future, we will investigate other FEM formulations for parameter reconstruction.

Acknowledgements

This work is supported by the NCCR Co-Me of the Swiss National Science Foundation and by the EU project BEAMING.

References

[1] C. B. Barber, D. P. Dobkin, and H. T. Huhdanpaa. The quickhull algorithm for convex hulls. *ACM T Math Software*, 22:469–483, 1996.

[2] C. Basdogan, S. De, J. Kim, M. Muniyandi, H. Kim, and M. A. Srinivasan. Haptics in minimally invasive surgical simulation and training. *IEEE Computer Graphics and Applications*, 24(2):56–64, 2004.

[3] B. Bickel, M. A. Otaduy, W. Matusik, H. Pfister, and M. Gross. Capture and modeling of non-linear heterogeneous soft tissue. *ACM Trans Graph*, 28:9, 2009.

[4] J.-D. Boissonnat and S. Oudot. Provably good sampling and meshing of surfaces. *Graphical Models*, 67:405–451, 2005.

[5] M. M. Doyley. Model-based elastography: a survey of approaches to the inverse elasticity problem. *Phys Med Biol*, 57(3):R35–73, 2012.

[6] H. Eskandari, S. E. Salcudean, R. Rohling, and J. Ohayon. Viscoelastic characterization of soft tissue from dynamic finite element models. *Phys Med Biol*, 53(22):6569–6590, 2008.

[7] N. Famaey and J. V. Sloten. Soft tissue modelling for applications in virtual surgery and surgical robotics. *Computer Methods in Biomechanics and Biomedical Engineering*, 11(4):351–366, 2008.

[8] O. Goksel and S. E. Salcudean. Image-based variational meshing. *IEEE Trans Med Imag*, 30(1):11–21, Jan 2011.

[9] A. Haddadi and K. Hashtrudi-Zaad. Real-time identication of huntcrossley dynamic models of contact environments. *IEEE Trans Robotics*, 28(3):555–566, 2012.

[10] R. Höver, G. Kósa, G. Székely, and M. Harders. Data-driven haptic rendering – from viscous fluids to viscoelastic solids. *IEEE Trans Haptics*, 2(1):15–27, 2009.

[11] F. Kallel and M. Bertrand. Tissue elasticity reconstruction using linear perturbation method. *IEEE Trans Med Imag*, 15:299–313, 1996.

[12] M. Kauer, V. Vuskovic, J. Dual, G. Szekely, and M. Bajka. Inverse finite element characterization of soft tissues. *Med Imag Anal*, 6:275–287, 2002.

[13] M. Kazhdan, M. Bolitho, , and H. Hoppe. Poisson surface reconstruction. In *Proc Eurographics Symp on Geom Proc*, pages 61–70, 2006.

[14] S. Misra, K. J. Macura, K. T. Ramesh, and A. M. Okamura. The importance of organ geometry and boundary constraints for planning of medical interventions. *Med Eng Phys*, 31(2):195–206, 2009.

[15] A. M. Okamura, K. J. Kuchenbecker, and M. Mahvash. Measurement-based modeling for haptic rendering. In *Haptic Rendering*. 2008.

[16] D. K. Pai, K. v. d. Doel, D. L. James, J. Lang, J. E. Lloyd, J. L. Richmond, and S. H. Yau. Scanning physical interaction behavior of 3D objects. In *Proc. Comp Graphics (SIGGRAPH)*, pages 87–96, 2001.

[17] A. Samani, J. Bishop, C. Luginbuhl, and D. B. Plewes. Measuring the elastic modulus of ex-vivo small tissue samples. *Phys Med Bio*, 48:2183–2198, 2003.

[18] E. Samur, M. Sedef, C. Basdogan, L. Avtan, and O. Duzgun. A robotic indenter for minimally invasive measurement and characterization of soft tissue response. *Med Imag Anal*, 11:361–373, 2007.

[19] J. R. Shewchuk. What is a good linear element? interpolation, conditioning, and quality measures. In *Int Meshing Roundtable*, 2002.

[20] D. Valtorta and E. Mazza. Dynamic measurements of soft tissue viscoelastic properties with a torsional resonator device. In *Proc Med Imag Comp Comp Asst Interv (MICCAI)*, pages 284–292, 2004.

[21] E. P. Westebring - VanDerPutten, R. H. M. Goossens, J. J. Jakimowicz, and J. Dankelman. Haptics in minimally invasive surgery – a review. *Minimally Invasive Therapy*, 17:3–16, 2008.

[22] T. Yamamoto, B. Vagvolgyi, K. Balaji, L. L. Whitcomb, and A. M. Okamura. Tissue property estimation and graphical display for teleoperated robot-assisted surgery. In *Proc. IEEE ICRA*, 2009.

[23] S. Yim and S. Choi. Shape modeling of soft real objects using force-feedback haptic interface. In *IEEE Hap Symp*, pages 479–484, 2012.

[24] Y. Zhu, T. J. Hall, and J. Jiang. A finite-element approach for youngs modulus reconstruction. *IEEE Trans Med Imag*, 22(7):890–901, 2003.

[25] O. C. Zienkiewicz and R. L. Taylor. *The Finite Element Method*. Butterworth-Heinemann, 2000.